Robust spin-orbit coupling in semimetallic $SrIrO_3$ under hydrostatic pressure

D. Fuchs [1,*] A. K. Jaiswal [1] F. Wilhelm,[2] D. Wang [3] A. Rogalev,[2] and M. Le Tacon [1]

[1] *Karlsruhe Institute of Technology, Institute for Quantum Materials and Technologies, Kaiserstraße 12, 76131 Karlsruhe, Germany*

[2] *ESRF-European Synchrotron Radiation Facility, 38043 Grenoble, France*

[3] *Karlsruhe Institute of Technology, Institute of Nanotechnology and Karlsruhe Nano Micro Facility (KNMFi), Kaiserstraße 12, 76131 Karlsruhe, Germany*

(Received 18 September 2024; revised 11 December 2024; accepted 4 February 2025; published 19 February 2025)

The semimetallic behavior of the perovskite iridate $SrIrO_3$ shifts the end member of the strongly spin-orbit (SO) coupled Ruddlesden-Popper series $Sr_{n+1}Ir_nO_{3n+1}$ away from the Mott insulating regime and the half-filled pseudospin $J_{\text{eff}} = \frac{1}{2}$ ground state well established in the layered iridates ($n = 1$ and 2). To investigate the robustness of the SO coupled ground state of $SrIrO_3$, x-ray absorption spectroscopy was carried out at the Ir $L_{2,3}$ edges under hydrostatic pressure up to 50 GPa at room temperature. The effective SO coupling was deduced from the branching ratio (BR) of the Ir L_2 and L_3 white lines. With increasing pressure, the BR decreases, and the Ir $L_{2,3}$ peak positions shift to higher energies. The number of $5d$ holes remains constant, indicating that the spectral weight redistribution and peak shifts arise from orbital mixing between t_{2g} and e_g related states. The expectation value of the angular part of the SO operator $\langle \text{LS} \rangle$ decreases by $\sim$15% at 50 GPa. This reduction, which is very similar to that observed in the layered iridates, is well explained by an increase of the octahedral crystal field due to the shortening of the Ir-O bond length under compression. Consistent with theoretical predictions, the orbital mixing and $\langle \text{LS} \rangle$ decrease as the crystal field increases. However, the effective SO coupling remains robust against pressure and does not indicate a covalency-driven breakdown within the investigated pressure range.

DOI: 10.1103/PhysRevB.111.075142

I. INTRODUCTION

When the spin and angular momentum of electrons are strongly coupled due to the relativistic spin-orbit (SO) interaction, the total angular momentum J becomes the relevant quantum number for describing the system. As the strength of SO coupling (SOC) increases with the atomic number Z, it emerges as a significant energy scale in the low-energy physics of $4d$ and $5d$ transition metals. There, SOC can give rise to exotic electronic and magnetic quantum states with nontrivial band topologies, including spin liquids [1,2], topological Mott insulators [3], Weyl semimetals, and axion insulators [4].

In the $5d$ transition metal oxides $Sr_{n+1}Ir_nO_{3n+1}$, the SOC strength becomes comparable with the Coulomb interaction and the crystal electric field (CF) splitting. Consequently, the ground state of the Ir^{4+} ion in the cubic CF ($10Dq$) of the IrO_6 octahedra is often well described by a pseudospin $J_{\text{eff}} = \frac{1}{2}$ picture [5–8]. For $n = 1$ or 2 layered members of this series, electron correlation and magnetic exchange interactions result in an antiferromagnetic (AFM) ground state. This leads to a splitting of the $J_{\text{eff}} = \frac{1}{2}$ state into lower and upper Hubbard bands, producing a SO Mott insulator [7,8]. In contrast, the end member of the Ruddlesden-Popper series $SrIrO_3$ (SIO; $n = \infty$) exhibits metallic behavior [9,10]. In the conventional framework, the increased coordination and dimensionality of the IrO_2 layers are expected to broaden the electronic bands, leading to greater band hybridization than the layered compounds. However, photoemission spectroscopy reveals a surprisingly narrow bandwidth in SIO ($\approx$0.3 eV), comparable with that of Sr_2IrO_4 (0.3–0.8 eV) [11]. This has been attributed to the pronounced orthorhombic distortion and rotation of the IrO_6 octahedra in SIO. Alternatively, it has been proposed that the metallic behavior of SIO arises from the absence of AFM order and a weaker electron correlation (U), which in the layered iridates is sufficient to open a Mott-Hubbard gap even for small U [12]. In contrast with the Mott scenario, where SIO is described by a single half-filled band, this perspective suggests the presence of multiple partially occupied bands with mixed orbital character.

A highly effective technique to probe the SO coupled ground state of iridates is x-ray absorption near-edge spectroscopy (XANES) at the Ir $L_{2,3}$ edge. This approach, proposed by van der Laan and Thole [13], relates the intensity ratio I_{L_3}/I_{L_2} of the L_3 and L_2 white lines (WLs) which are split by SOC to the expectation value of the angular part of the SO operator $\langle \text{LS} \rangle$ [13–15]. According to the SO sum rules, the branching ratio (BR*) for the $p \rightarrow d$ transitions is given by: $\text{BR}^* = I_{L_3}/I_{L_2} = (2 + r)/(1-r)$, where $r = \langle \text{LS} \rangle / \langle n_h \rangle$, and $\langle n_h \rangle$ is the average number of $5d$ holes [13].

XANES studies on various Ir-based $5d$ compounds, including Sr_2IrO_4, IrO_2, or $IrCl_3$, have revealed strong SOC largely

*Contact author: dirk.fuchs@kit.edu

independent of chemical composition, crystal structure, or electronic state [16,17]. These materials exhibit a BR* of ∼7, significantly higher than the statistical value of 2, which corresponds to system with $\langle LS\rangle = 0$ and is solely determined by the $p_{1/2}$ and $p_{3/2}$ electron occupation. For metallic Ir and Ir alloys, BR* is much smaller (≈3.5), indicating substantial quenching of $\langle LS\rangle$, likely caused by the increased bandwidth induced by $5d$ hybridization [16,18]. However, orbital moment quenching $\langle LS\rangle = 0$ does not necessarily imply the absence of SO interaction in the Hamiltonian $H_{SO} = \zeta \times L \cdot S$, where ζ is the SOC constant/energy. When SOC dominates ($\zeta \gg 10Dq$), the Ir $5d$ states split into $5d_{5/2}$ and $5d_{3/2}$ states, with L_2 and L_3 absorption corresponding to transitions $2p_{1/2} \rightarrow 5d_{3/2}$ and $2p_{3/2} \rightarrow 5d_{3/2,5/2}$, respectively: Notably, $I_{L_2} = 0$ for $Ir^{4+}(5d^5)$, which is inconsistent with observations in iridates. Furthermore, the ground state is often well described by the pseudospin scenario. In the strong SOC limit ($\zeta \leqslant 10Dq$), the octahedral CF splits the $5d$ states into e_g and t_{2g} states, with t_{2g} further split by SOC into a fully occupied $J_{\text{eff}} = \frac{3}{2}$ quadruplet and a half-filled $J_{\text{eff}} = \frac{1}{2}$ doublet. Note that, in this case, orbital mixing between the e_g and t_{2g} states is generally neglected.

Hydrostatic pressure p offers a powerful means to tune electronic bandwidth, octahedral distortions/rotations, and CF, making it ideal for studying $\langle LS\rangle$ and the SO coupled ground state in SIO. The layered iridates exhibit a robust $J_{\text{eff}} = \frac{1}{2}$ ground state with only moderate quenching of $\langle LS\rangle$ under increasing p [19,20]. However, with greater connectivity of IrO_6 octahedra occurring, e.g., when going from corner-sharing to edge- or face-sharing configurations, the reduced Ir-Ir distance facilitates molecular orbital formation and the breakdown of the $J_{\text{eff}} = \frac{1}{2}$ ground state [8]. Covalency-driven orbital mixing thus plays a critical role in shaping the pseudospin scenario in iridates, motivating detailed studies of SIO under p.

The availability of bulk SIO is limited by the impossibility of producing single crystals under ambient p [21,22]. Nevertheless, single-crystalline SIO can be synthesized as epitaxial thin films, where the orthorhombic structure is stabilized by strain [23–27]. Using pulsed laser deposition, we have successfully grown SIO films on a water-soluble $Sr_4Al_2O_7$ sacrificial layer, enabling the preparation of structurally relaxed freestanding single-crystalline SIO films. This approach has allowed us to study the SO coupled ground state of bulk-like SIO. We performed Ir $L_{2,3}$ x-ray absorption spectroscopy (XAS) under hydrostatic p, analyzing the BR and $\langle LS\rangle$ as a function of p at room temperature. The Ir $L_{2,3}$ XANES indicates a rather large value of $\langle LS\rangle$ at ambient p, suggesting significant mixing of $J_{\text{eff}} = \frac{3}{2}$ and e_g orbitals. With increasing p, $\langle LS\rangle$ decreases, consistent with the CF enhancement due to a p-induced shortening of the Ir-O bond length. Despite the semimetallic character of SIO, the p-induced changes in $\langle LS\rangle$ are remarkably like those observed in the layered insulating iridates Sr_2IrO_4 and $Sr_3Ir_2O_7$, indicating a robust $J_{\text{eff}} = \frac{1}{2}$ ground state for SIO.

II. EXPERIMENTAL

Single-crystalline SIO was produced by the thin-film deposition technique [28]. To this end, epitaxial SIO films with a thickness of ∼120 nm were deposited by pulsed laser deposition on a water-soluble $Sr_4Al_2O_7$ thin film which was first grown epitaxially on a (001) $SrTiO_3$ substrate, see Supplemental Material [29]. The films were removed from the substrate and transferred to a thermal release tape, attached to the SIO surface before, by dissolving the water-soluble sacrificial layer. Finally, the SIO single-crystal-like freestanding membranes were transferred to the diamond culets of the used diamond anvil cells by stamping the membranes onto the culet surface under the load of heat and weight, see Supplemental Material [29]. Using membrane-driven partially perforated diamond anvil cells with 600 and 350 μm culet, hydrostatic p could be continuously varied up to 50 GPa. The cells were filled with He gas and sealed with steel gaskets. Then p was measured *in situ* using ruby fluorescence. The XANES at the Ir $L_{2,3}$ edge was done at the beam line ID12 at the European Synchrotron Radiation Facility in Grenoble, France. Measurements were carried out using circular polarized light with normal beam incidence at room temperature using the HU-38 undulator and an energy-resolved detector. All the spectra were recorded using the partial fluorescence yield with two silicon drift detectors with a Falcon X signal processor. Due to the low thickness of the film (120 nm), no reabsorption corrections were needed. Further information on data analysis is described in the Supplemental Material [29].

III. RESULTS

A. Structural properties of $SrIrO_3$

The structural characterization of the SIO freestanding films was carried out by x-ray diffraction (XRD) and scanning transmission electron microscopy (STEM). Symmetric $\theta/2\theta$ diffraction, shown in Fig. 1(a), confirmed the (110) growth orientation of the freestanding film. The orthorhombic structure was further characterized by probing asymmetric reflections of the pseudocubic types ⟨113⟩ and ⟨123⟩. Half-integer reflections, indicative of a doubling of the pseudocubic unit cell, were observed for every reflection except for (312), as shown in Fig. 1(b). These observations allowed the deduction of the octahedral rotation pattern characteristic of the orthorhombic structure. For the out-of-plane film axis, only antiphase rotation (−) was observed, whereas for the in-plane axes, both in-phase (+) and antiphase (−) rotations were present. This pattern is consistent with in-plane twinning of the orthorhombic c axis, expected due to epitaxial growth on the quadratic surface cells of $Sr_4Al_2O_7$ and $SrTiO_3$. According to Glazer notation, the octahedral tilt pattern is $(a^-a^-c^+)$, identical to that of bulk orthorhombic (*Pbnm*) SIO [22,30].

Plan-view high-resolution (HR) STEM images and corresponding fast Fourier transforms [Fig. 1(c)] also confirm the orthorhombic structure with the c axis aligned perpendicular to the surface normal. The integrated differential phase contrast (iDPC) STEM image [Fig. 1(d)] further reveals the antiphase rotation along the out-of-plane direction, evidenced by elongated oxygen atom columns [blue ellipses in Fig. 1(d)] resulting from antiphase-rotated octahedra. The antiphase rotation was estimated to (−)≈8°. Lattice parameters deduced from XRD (see Supplemental Material [29]) are $a = 5.61(1)$ Å, $b = 5.60(5)$ Å, and $c = 7.91(6)$ Å. These parameters and rotation angles align well with those

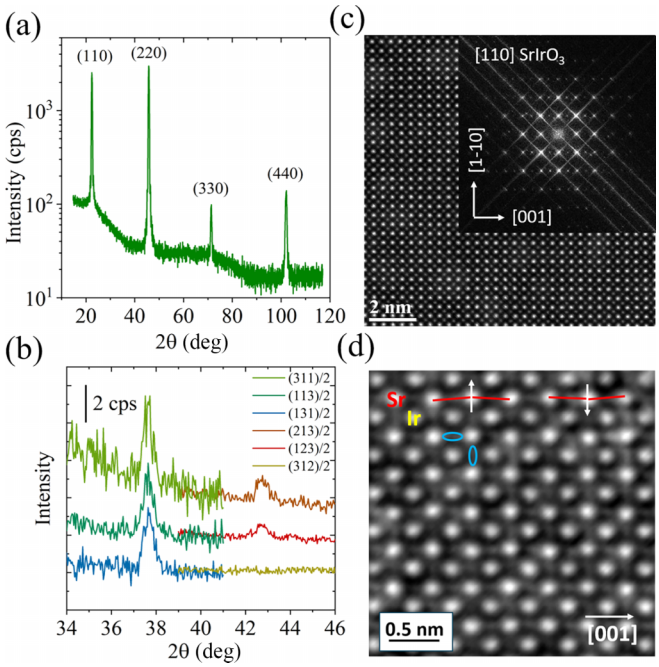

FIG. 1. Structural properties of SIO freestanding films. (a) Symmetric $\theta/2\theta$ scan with respect to surface normal, indicating pure (110) growth orientation. (b) The half-integer reflections of the pseudocubic ⟨113⟩ and ⟨123⟩ peaks. (312)/2 peak indicating (+) rotation for the out-of-plane direction is absent. The peaks are shifted vertically for clarity. The pseudocubic axes a, b, and c correspond to the orthorhombic [1–10], [001], and [110] directions, respectively. (c) Plan-view high-resolution scanning transmission electron microscopy (HR-STEM) image and the corresponding fast Fourier transformation in inset. (d) Integrated differential phase contrast (iDPC)-STEM image, showing untwinned domain with in-plane alignment of the c axis and (−) rotation along the out-of-plane direction. Red lines and blue ellipses indicate Sr and O displacement, respectively.

observed for the high-p phase of SIO synthetized at 6 GPa [$a = 5.60$ Å, $b = 5.57$ Å, $c = 7.90$ Å, (+) = 8.7°, and (−) = 12°] [31]. The slightly smaller lattice parameters and larger rotation angles are likely explained by the high-p synthesis conditions [22].

B. XAS at the Ir $L_{2,3}$ edge

The p dependence of ⟨LS⟩ in SIO was investigated by XAS. XANES spectra at the Ir $L_{2,3}$ edge were recorded under hydrostatic p ranging from 0.37 to 47.4 GPa at room temperature. The most notable feature in the Ir L_2 and L_3 XANES spectra is the sharp WL corresponding to the $2p_{1/2} \rightarrow 5d_{3/2}$ and $2p_{3/2} \rightarrow 5d_{3/2,5/2}$ electronic transitions, respectively. Figure 2 shows the normalized intensity (see Supplemental Material [29]) of the Ir $L_{2,3}$ XANES across the p range. The WL intensity of the Ir L_3 XANES decreases markedly with p, while that of the L_2 XANES increases only slightly. The extended x-ray absorption fine structure (EXAFS) oscillations observed after the WL shift to higher energies with increasing p, indicative of a shortening of the interatomic distances between Ir and the next-nearest oxygen atoms, as expected under compression [32,33]. The energy shift of the EXAFS

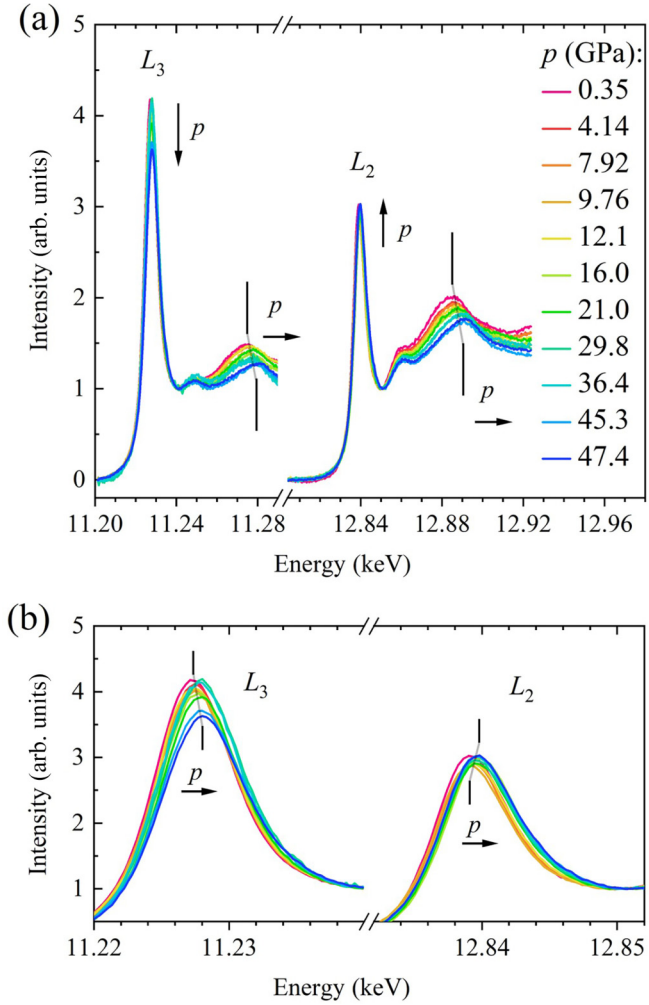

FIG. 2. (a) Normalized intensity of the Ir L_3 and L_2 x-ray absorption near-edge spectroscopy (XANES) of SIO for different p's ranging from 0.35 to 47.4 GPa. Measurements were taken in normal beam incidence (90°) at $T = 300$ K. With increasing p, the peak intensity of L_3 decreases and L_2 increases, as indicated by the arrows. The extended x-ray absorption fine structure (EXAFS) feature after the white lines (WLs; indicated by bars) also shifts to higher energy with increasing p. (b) Enlarged view on the L_3 and L_2 WLs to visualize p dependence of the intensity and peak position. Color scale is the same as above.

oscillations is similar at both edges (L_3 and L_2) and amounts to ∼7.5 eV at $p = 47.4$ GPa. However, due to p-dependent variations in the background absorption, accurate determination of the EXAFS maximum was challenging. The energy E_0, corresponding to the maximum of the $L_{2,3}$ WL also shifts, albeit by a smaller amount (≈0.8 eV) than the EXAFS oscillations. Nevertheless, both features—WL and EXAFS—shift nearly linearly with p, indicating continuous changes in the electronic and local structural properties of the IrO_6 octahedra [see Fig. 3(a)].

Next, we quantify the effect of SOC on the 5d states through the BR of the WL integrals at the SO split absorption edges for the $p \rightarrow d$ transitions. The BR is defined as $I_{L3}^{XAS}/(I_{L3}^{XAS} + I_{L2}^{XAS})$, where $I_{L2,3}^{XAS}$ represent the integrated WL intensities, determined after subtraction of the background

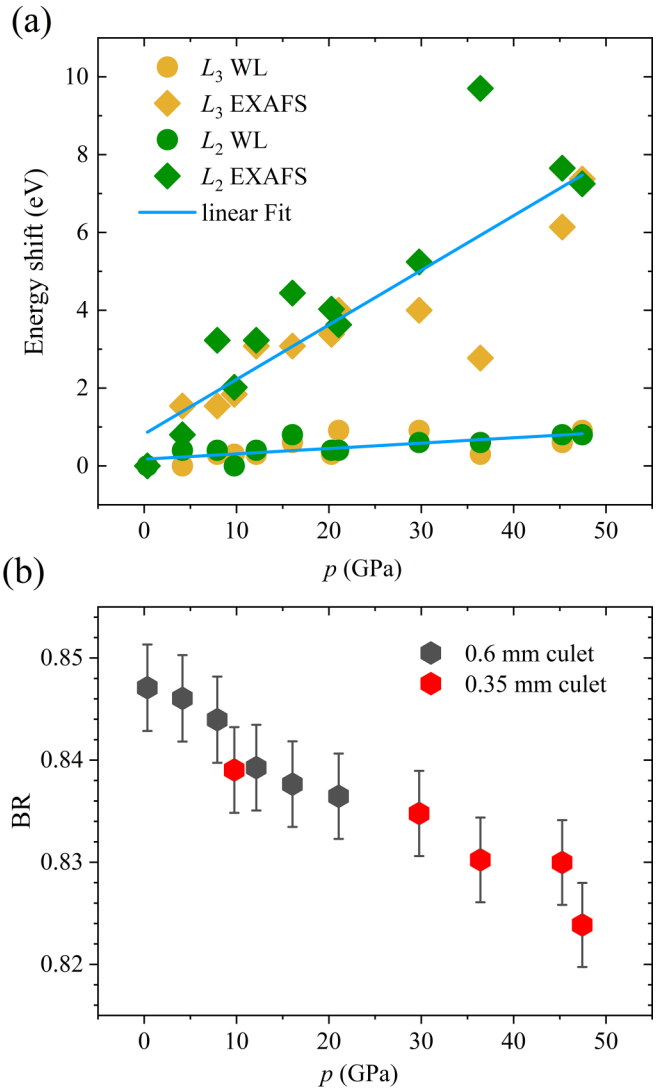

FIG. 3. (a) Energy shift of the peak position E_0 of the Ir L_3 and L_2 white lines (WLs) and extended x-ray absorption fine structure (EXAFS) wiggles vs hydrostatic pressure p. The energy shifts nearly linear with p and amounts to ∼0.8 and 7.5 eV for the WL and EXAFS features, respectively, at $p = 47$ GPa. (b) The branching ratio (BR) $= I_{L3}^{\mathrm{XAS}}/(I_{L3}^{\mathrm{XAS}} + I_{L2}^{\mathrm{XAS}})$ vs p. Measurements were obtained from different diamond anvil cells, see legend. Error bars are related to WL area analysis.

using an arctangent function, see Supplemental Material [29]. This ratio is related to the expectation value of the angular part of the ground-state SO operator ⟨LS⟩ through the SO sum rules: BR $= \frac{2}{3} + \langle \mathrm{LS}\rangle/(3 + n_{\mathrm{h}})$ [17]. As already suggested by Fig. 2, I_{L3}^{XAS} decreases while I_{L2}^{XAS} increases with p. This trend is consistent with observations in Sr_2IrO_4 and $Sr_3Ir_2O_7$ [19,20]. The sum $I_{L3}^{\mathrm{XAS}} + I_{L2}^{\mathrm{XAS}}$, which is proportional to the number of Ir $5d$ holes $n_h = n_h^{j=3/2} + n_h^{j=5/2} \approx 5$, remains nearly constant with p, see Supplemental Material [29]. Therefore, the shift in spectral weight from I_{L3}^{XAS} to I_{L2}^{XAS} with increasing p suggests a progressive mixing or hybridization of occupied $5d_{3/2}$—and unoccupied $5d_{5/2}$—states.

Figure 3(b) shows the BR as a function of p. At moderate $p < 5$ GPa, the BR (≈0.846) is comparable with that of compressively strained epitaxial SIO films (BR≈0.844), investigated in previous studies [34]. The observed BR is significantly higher than the statistical value of $\frac{2}{3}$ ($\langle \mathrm{LS}\rangle = 0$), indicating the presence of strong SOC effects. This BR is consistent with values reported for other Ir compounds such as $Sr_3Ir_2O_7$, Sr_2IrO_4, IrO_2, or $IrCl_3$ [16,19,20]. Notably, small deviations in BR can arise from differences in methods for the WL peak area extraction; however, the use of a consistent procedure ensures the robustness of our conclusions. With increasing p, the BR steadily decreases to 0.824 for $p = 47$ GPa, indicating a continuous reduction in ⟨LS⟩. Importantly, this decrease is gradual, with no abrupt changes or drops indicative of orbital momentum quenching.

IV. DISCUSSION

In perovskite iridates, the SOC energy of the $5d$ electrons (ζ) competes with the CF energy. The large spatial extension of the $5d$ orbitals results in large $10Dq$ (≈3 eV) [35,36], which usually results in a low spin $S = \frac{1}{2}$ ground state in the limit of weak SOC. However, strong SOC of Ir ($\zeta = 0.45$ eV) [37–39] splits t_{2g} into a fully occupied $J_{\mathrm{eff}} = \frac{3}{2}$ quadruplet and a half-filled $J_{\mathrm{eff}} = \frac{1}{2}$ doublet. In such a ground state, the contribution of holes to the expectation value $\langle \mathrm{LS}\rangle = -\frac{1}{2}$ $[j_{\mathrm{eff}}(j_{\mathrm{eff}}+1) - l_{\mathrm{eff}}(l_{\mathrm{eff}}+1) - s(s+1)]$ is given by the sum of the SO values $\langle \mathrm{LS}\rangle J_{\mathrm{eff}} = \frac{3}{2}$ (=0) and $\langle \mathrm{LS}\rangle J_{\mathrm{eff}} = \frac{1}{2}$ (=1), resulting in BR = 0.73, which is significantly smaller than what we observed [Fig. 3(a)]. In this scenario, only the SOC-induced mixing within the t_{2g} manifold is considered ($\zeta < 10Dq$, see Supplemental Material [29]). However, when ζ becomes comparable with $10Dq$, the mixing between t_{2g} and e_g states in the fully diagonalized SOC Hamiltonian scales with $\zeta/(\zeta/2 + 10Dq)$, allowing up to 20% occupancy of orbitals that are typically unoccupied [40]. Configuration interaction calculations for an Ir^{4+} ion in an octahedral CF also reveal significant mixing between the $J_{\mathrm{eff}} = \frac{3}{2}$ and e_g states [41]. In addition to the contributions of the $J_{\mathrm{eff}} = \frac{1}{2}$ state to ⟨LS⟩, orbital mixing between the symmetry-equivalent $J_{\mathrm{eff}} = \frac{3}{2}$ and e_g states also results in a contribution of e_g states to ⟨LS⟩. The subsequent increase of ⟨LS⟩ follows the scaling relation $\zeta/10Dq$. For example, with $\zeta = 0.3$ eV and $10Dq = 3$ eV, the calculated total ⟨LS⟩ aligns closely with the value inferred from the experimental BR [41,42].

The large BR and p-induced changes in the Ir $L_{2,3}$ XANES of SIO reported here therefore strongly suggest the presence of orbital mixing of $J_{\mathrm{eff}} = \frac{3}{2}$ and e_g states. It is important to note that noncubic structural distortions, such as tetragonal CF splitting Δ_t can also influence the BR and the electronic ground state when it becomes comparable with ζ [6]. For comparison in the layered iridates Sr_2IrO_4 or $Sr_3Ir_2O_7$, Δ_t amounts to 1.6 and 1.9 eV [36], respectively, considerably exceeding ζ.

With increasing p, the BR progressively decreases to 0.824 for $p = 47$ GPa, reflecting a continuous reduction of ⟨LS⟩. This is illustrated in Fig. 4(a), where we have extracted the p dependence of ⟨LS⟩ from the BR. The expectation value ⟨LS⟩ decreases by ∼15% and signals a significant reduction in orbital angular momentum. Under increasing p, the Ir-O bond length is expected to shorten. For example, in Sr_2IrO_4,

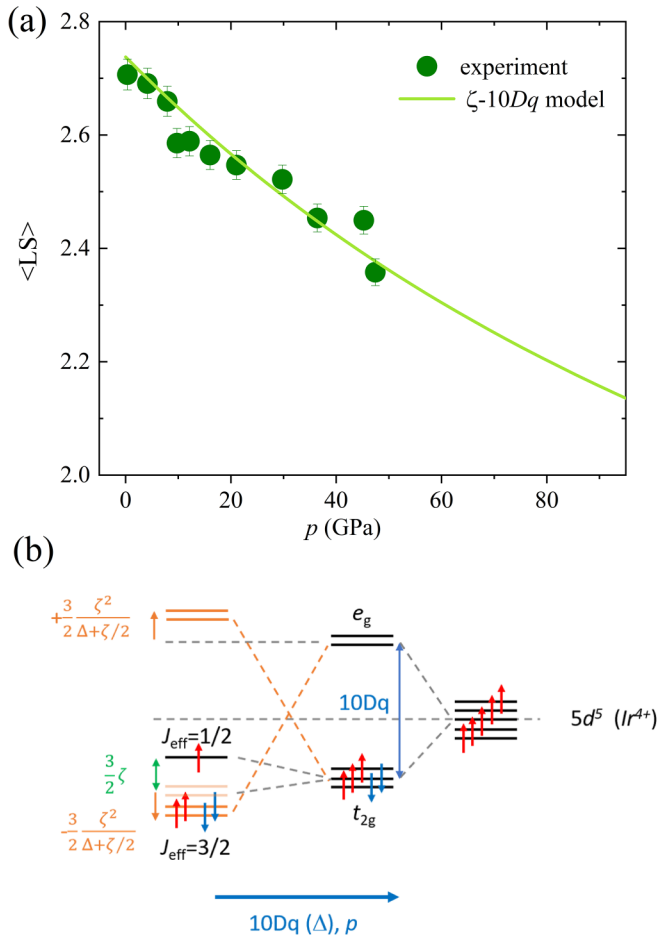

FIG. 4. (a) Effective spin-orbit coupling (SOC) as deduced from the branching ratio (BR) of $SrIrO_3$. Error bars are related to white line (WL) area analysis. The solid line indicates calculated values of $\langle LS \rangle$ based on the ζ-$10Dq$ model of Donnerer *et al.* [20], see Supplemental Material [29]. (b) Energy level scheme of the Ir $5d$ states split by crystal electric field (CF) and SOC. The $5d$ states are split by the octahedral CF $10Dq$ (right) and are then further split by SOC ζ (left) into $J_{\text{eff}} = \frac{1}{2}$ and $\frac{3}{2}$ states. In the limit of $\zeta \leqslant 10Dq$, e_g-t_{2g} orbital mixing results in an energy shift of the $J_{\text{eff}} = \frac{3}{2}$ (e_g) states by $-(+)\frac{3}{2} \times \zeta^2/(10Dq + \zeta/2)$ [40]. With increasing pressure p, $10Dq$ increases, yielding a decrease of $\langle LS \rangle$.

the a-lattice parameter contracts by $\sim -0.15\%$/GPa, leading to an estimated 50% enhancement of the CF strength at $p = 70$ GPa [19].

To probe the p dependence of $\langle LS \rangle$ in relation to the p-induced increase of $10Dq$, we employed the ζ-$10Dq$ model, proposed by Donnerer *et al.* [20]. This single-ion model incorporates SOC and CF, with a complete diagonalization of the Hamiltonian that fully accounts for the mixing between the t_{2g} and e_g states. The model requires only one adjustable parameter, $\zeta/10Dq$, to calculate $\langle LS \rangle$, see Ref. [20] and Supplemental Material [29]. Following the literature, we used $\zeta = 0.3$ eV [41], while $10Dq$ at $p \approx 0$ was adjusted to 1.7 eV to reproduce the experimental value of $\langle LS \rangle = 2.7$. This CF strength is consistent with first-principles calculations for SIO [43] and is distinctly smaller than experimental values reported for Sr_2IrO_4 (3.8 eV) and $Sr_3Ir_2O_7$ (3.55 eV) [36]. The lower $10Dq$ for SIO compared with layered iridates can be attributed to its metallic nature and the absence of Mott splitting in the $J_{\text{eff}} = \frac{1}{2}$ state. In Sr_2IrO_4, the Coulomb repulsion splits the $J_{\text{eff}} = \frac{1}{2}$ doublet by ~ 2 eV, lowering the occupied $J_{\text{eff}} = \frac{1}{2}$ state by ~ 1 eV and thereby increasing the effective e_g-t_{2g} splitting, i.e., $10Dq$ by a similar amount [44,45]. This explanation is supported by the comparable Ir-O bond distances in the rigid IrO_6 octahedra across these materials [31,37], while the electronic bandwidth near the Fermi energy, which is similar for SIO and Sr_2IrO_4 [27], is unlikely to significantly affect $10Dq$. The p-induced decrease in $\langle LS \rangle$ is therefore most likely driven by an increase in the CF due to the hydrostatic compression of SIO and the disentanglement of $J_{\text{eff}} = \frac{3}{2}$ and e_g states with increasing p.

Further experimental support for this scenario is also provided by the observed upshift of E_0. For $p = 47$ GPa, the E_0 positions of the L_3 and L_2 WLs shift by ~ 0.8 eV to higher energies, consistent with observations for $Sr_3Ir_2O_7$ under similar conditions [20]. Since the number of $5d$ holes remains nearly constant, varying by $< 5\%$, the shift in E_0 is most likely driven by CF effects and orbital mixing. According to XANES selection rules, the mixing of $J_{\text{eff}} = \frac{3}{2}$ and e_g states allows transitions to empty e_g states at both L_2 and L_3 edges, which are forbidden for the L_2 edge in the absence of orbital mixing. An increase of CF by $\delta 10Dq$ raises the energy of the e_g states, leading to an upshift of the L_2 and L_3 WLs of similar magnitude. At $p = 47$ GPa, CF is expected to increase from 1.7 to 2.3 eV, see Supplemental Material [29]. Albeit smaller, the calculated shift is on the same order of magnitude as the observed one, further supporting the orbital-mixing scenario. Additionally, tight-binding calculations predict an upshift of the $J_{\text{eff}} = \frac{3}{2}$ state with increasing $10Dq$ [40]. A corresponding energy level diagram illustrating this is provided in Fig. 4(b).

To gain further insights on the influence of CF strength on $\langle LS \rangle$, it is instructive to compare the p-induced changes of the Ir L_2 and L_3 XANES of SIO, Sr_2IrO_4, and $Sr_3Ir_2O_7$ that exhibit notable similarities up to ~ 50 GPa. Specifically, I_{L3}^{XAS} decreases while I_{L2}^{XAS} increases with p. Figure 5 shows relative change of $\langle LS \rangle$ as derived from the BR as a function of p for SIO compared with reported data [19,20] for the layered iridates Sr_2IrO_4 and $Sr_3Ir_2O_7$. The figure also includes simulations of $\langle LS \rangle$ for $\zeta = 0.3$ eV and $10Dq = 1.2$, 1.7, and 2.7 eV, corresponding to $\pm 20\%$ variations from the extracted ambient p value for SIO. In the moderate p regime ($p < 50$ GPa), these simulations clearly suggest only minor dependence of the relative p-induced decrease of $\langle LS \rangle$ on the strength of cubic CF $10Dq$.

Although experimental BR and $\langle LS \rangle$ are reasonably well described by p-induced changes of the cubic CF $10Dq$ and resulting orbital mixing of e_g and t_{2g} states in the low-p regime [19,20], significant deviations emerge for the layered iridates at higher p. For Sr_2IrO_4, deviations are evident >50 GPa, and for $Sr_3Ir_2O_7$, deviations are already apparent for 10 GPa. The simulations indicate that the larger $10Dq$ values of the layered iridates, e.g., 3.8 and 3.55 eV for insulating Sr_2IrO_4 and $Sr_3Ir_2O_7$, respectively, or 2.9 eV for nonmetallic $BaIrO_3$ [41], are insufficient to account for these deviations. Instead, the observed discrepancies are more likely attributed to tetragonal distortion and noncubic CF effects, which can contribute to the quenching of $\langle LS \rangle$. Additionally, a struc-

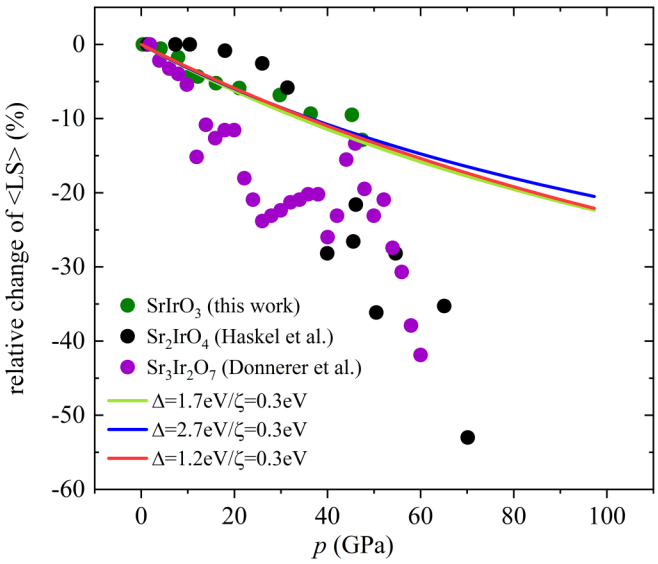

FIG. 5. Relative change of ⟨LS⟩ for the perovskite-related iridates $SrIrO_3$, Sr_2IrO_4, and $Sr_3Ir_2O_7$. Additional data were taken from Refs. [19,20]. Solid lines indicate simulations from the ζ-$10Dq$ model for $\zeta = 0.3$ eV and $10Dq$ (Δ) = 1.2, 1.7, and 2.7 eV.

tural phase transition in $Sr_3Ir_2O_7$ around 53 GPa [46] could influence both the CF splitting and the BR. For $p > 50$ GPa, enhanced hybridization effects and bandwidth-driven orbital mixing may also become significant [19,46]. Unfortunately, the diamond anvil cells used in our experiment did not allow measurements for $p > 50$ GPa, leaving the high-p behavior of SIO unexplored.

We conclude that the robustness of ⟨LS⟩ in SIO in the investigated p range can likely be attributed to the absence of significant noncubic CF and of hybridization effects. Compounds with face-sharing (edge-sharing) IrO_6 octahedra and short d_{Ir-Ir}≈2.3 Å (≈2.8 Å), compared with that of the corner-sharing case of SIO (≈3.96 Å), exhibit a covalency-driven collapse of the $J_{\text{eff}} = \frac{1}{2}$ state [8]. For metallic Ir (d_{Ir-Ir}≈2.6 Å), the BR at ambient conditions is close to the statistical value [16], indicating strong quenching of ⟨LS⟩. In contrast, the narrow electronic bandwidth and relatively large Ir-Ir distance ($d_{Ir-Ir} \approx 3.96$ Å) in SIO minimize the direct overlap of neighboring 5d orbitals, effectively preventing the formation of molecular orbitals by covalency and preserving the $J_{\text{eff}} = \frac{1}{2}$ pseudospin state.

V. SUMMARY

In summary, the synthesis of orthorhombic perovskite SIO as freestanding thin-film material enabled a systematic investigation of the effective SOC in the corner-sharing IrO_6 octahedra under hydrostatic p and an evaluation of the $J_{\text{eff}} = \frac{1}{2}$ ground-state scenario. The angular part of the SO operator expectation value ⟨LS⟩ was derived from the BR of Ir $L_{2,3}$ XANES. At ambient p, the BR is relatively large (0.85), indicating a significant orbital mixing between the occupied $J_{\text{eff}} = \frac{3}{2}$ pseudospin (t_{2g}-related) states and unoccupied e_g states. Upon increasing p, ⟨LS⟩ decreases by ∼15% at $p \approx 50$ GPa. This p-induced reduction in the BR and ⟨LS⟩ reflects a suppression of the e_g-t_{2g} orbital mixing, consistent with an increase in the cubic CF parameter $10Dq$ caused by the shortening of the Ir-O bond length under compression. The cubic CF parameter for SIO, derived from the ζ-$10Dq$ model, is 1.7 eV at ambient p, which is notably smaller than the values reported for the layered iridates. This difference is likely attributed to the metallic nature of SIO and the absence of a Mott-driven splitting of the $J_{\text{eff}} = \frac{1}{2}$ doublet at ambient p. Despite this semimetallic character, the SOC-driven $J_{\text{eff}} = \frac{1}{2}$ ground state is found to be remarkably robust across the investigated p range. The results provide compelling evidence for the role of orbital mixing and the interplay of SOC and CF effects in shaping the electronic structure of SIO.

ACKNOWLEDGMENTS

We thank R. Eder for fruitful discussion and are grateful to R. Thelen and the Karlsruhe Nano-Micro Facility for technical support. A.K.J. acknowledges financial support from the European Union's Framework Programme for Research and Innovation, Horizon 2020, under the Marie Skłodowska-Curie Grant Agreement No. 847471 (QUSTEC).

[1] J. Chaloupka, G. Jackeli, and G. Khaliullin, Kitaev-Heisenberg model on a honeycomb lattice: Possible exotic phases in iridium oxides A_2IrO_3, Phys. Rev. Lett. **105**, 027204 (2010).

[2] A. Revelli, M. Moretti Sala, G. Monaco, C. Hickey, P. Becker, F. Freund, A. Jesche, P. Gegenwart, T. Eschmann, F. L. Buessen *et al.*, Fingerprints of Kitaev physics in the magnetic excitations of honeycomb iridates, Phys. Rev. Res. **2**, 043094 (2020).

[3] D. Pesin and L. Balents, Mott physics and band topology in materials with strong spin-orbit interaction, Nat. Phys. **6**, 376 (2010).

[4] X. Wan, A. M. Turner, A. Vishwanath, and S. Y. Savrasov, Topological semimetal and Fermi-arc surface states in the electronic structure of pyrochlore iridates, Phys. Rev. B **83**, 205101 (2011).

[5] S. Boseggia, R. Springell, H. C. Walker, H. M. Rønnow, Ch. Rüegg, H. Okabe, M. Isobe, R. S. Perry, S. P. Collins, and D. F. McMorrow, Robustness of basal-plane antiferromagnetic order and the $J_{\text{eff}} = \frac{1}{2}$ state in single-layer iridate spin-orbit mott insulators, Phys. Rev. Lett. **110**, 117207 (2013).

[6] M. Moretti Sala, S. Boseggia, D. F. McMorrow, and G. Monaco, Resonant x-ray scattering and the $J_{\text{eff}} = \frac{1}{2}$ electronic ground state in iridate perovskites, Phys. Rev. Lett. **112**, 026403 (2014).

[7] B. J. Kim, H. Ohsumi, T. Komesu, S. Sakai, T. Morita, H. Takagi, and T. Arima, Phase-sensitive observation of a spin-orbital Mott state in Sr_2IrO_4, Science (1979) **323**, 1329 (2009).

[8] M. Ye, H.-S. Kim, J.-W. Kim, C.-J. Won, K. Haule, D. Vanderbilt, S.-W. Cheong, and G. Blumberg, Covalency-driven collapse of strong spin-orbit coupling in face-sharing iridium octahedra, Phys. Rev. B **98**, 201105(R) (2018).

[9] G. Cao, V. Durairaj, S. Chikara, L. E. DeLong, S. Parkin, and P. Schlottmann, Non-Fermi-liquid behavior in nearly ferromagnetic $SrIrO_3$ single crystals, Phys. Rev. B **76**, 100402(R) (2007).

[10] J. Fujioka, T. Okawa, A. Yamamoto, and Y. Tokura, Correlated Dirac semimetallic state with unusual positive magnetoresistance in strain-free perovskite $SrIrO_3$, Phys. Rev. B **95**, 121102(R) (2017).

[11] J. K. Kawasaki, M. Uchida, H. Paik, D. G. Schlom, and K. M. Shen, Evolution of electronic correlations across the rutile, perovskite, and Ruddelsden-Popper iridates with octahedral connectivity, Phys. Rev. B **94**, 121104(R) (2016).

[12] B. J. Kim, Hosub Jin, S. J. Moon, J.-Y. Kim, B.-G. Park, C. S. Leem, Jaejun Yu, T. W. Noh, C. Kim, S.-J. Oh *et al.*, Novel $J_{\text{eff}} = \frac{1}{2}$ Mott state induced by relativistic spin-orbit coupling in Sr_2IrO_4, Phys. Rev. Lett. **101**, 076402 (2008).

[13] G. van der Laan and B. T. Thole, Local probe for spin-orbit interaction, Phys. Rev. Lett. **60**, 1977 (1988).

[14] B. T. Thole and G. van der Laan, Branching ratio in x-ray absorption spectroscopy, Phys. Rev. B **38**, 3158 (1988).

[15] B. T. Thole and G. van der Laan, Linear relation between x-ray absorption branching ratio and valence-band spin-orbit expectation value, Phys. Rev. A **38**, 1943 (1988).

[16] J. P. Clancy, N. Chen, C. Y. Kim, W. F. Chen, K. W. Plumb, B. C. Jeon, T. W. Noh, and Y.-J. Kim, Spin-orbit coupling in iridium-based 5*d* compounds probed by x-ray absorption spectroscopy, Phys. Rev. B **86**, 195131 (2012).

[17] K. S. Pedersen, J. Bendix, A. Tressaud, E. Durand, H. Weihe, Z. Salman, T. J. Morsing, D. N. Woodruff, Y. Lan, W. Wernsdorfer *et al.*, Iridates from the molecular side, Nat. Commun. **7**, 12195 (2016).

[18] Y. Jeon, B. Qi, F. Lu, and M. Croft, Transition-metal (Au, Pt, Ir, Re) bonding to Al,Si,Ge: X-ray-absorption studies, Phys. Rev. B **40**, 1538 (1989).

[19] D. Haskel, G. Fabbris, M. Zhernenkov, P. P. Kong, C. Q. Jin, G. Cao, and M. van Veenendaal, Pressure tuning of the spin-orbit coupled ground state in Sr_2IrO_4, Phys. Rev. Lett. **109**, 027204 (2012).

[20] C. Donnerer, M. M. Sala, S. Pascarelli, A. D. Rosa, S. N. Andreev, V. V. Mazurenko, T. Irifune, E. C. Hunter, R. S. Perry, and D. F. McMorrow, High-pressure insulator-to-metal transition in $Sr_3Ir_2O_7$ studied by x-ray absorption spectroscopy, Phys. Rev. B **97**, 035106 (2018).

[21] J. M. Longo, J. A. Kafalas, and R. J. Arnott, Structure and properties of the high and low pressure forms of $SrIrO_3$, J. Solid State Chem. **3**, 174 (1971).

[22] J. G. Zhao, L. X. Yang, Y. Yu, F. Y. Li, R. C. Yu, Z. Fang, L. C. Chen, and C. Q. Jin, High-pressure synthesis of orthorhombic $SrIrO_3$ perovskite and its positive magnetoresistance, J. Appl. Phys. **103**, 103706 (2008).

[23] F.-X. Wu, J. Zhou, L. Y. Zhang, Y. B. Chen, S.-T. Zhang, Z.-B. Gu, S.-H. Yao, and Y.-F. Chen, Metal-insulator transition in $SrIrO_3$ with strong spin-orbit interaction, J. Phys. Condens. Matter **25**, 125604 (2013).

[24] Z. T. Liu, M. Y. Li, Q. F. Li, J. S. Liu, W. Li, H. F. Yang, Q. Yao, C. C. Fan, X. G. Wan, Z. Wang *et al.*, Direct observation of the Dirac nodes lifting in semimetallic perovskite $SrIrO_3$ thin films, Sci. Rep. **6**, 30309 (2016).

[25] J. H. Gruenewald, J. Nichols, J. Terzic, G. Cao, J. W. Brill, and S. S. A. Seo, Compressive strain-induced metal–insulator transition in orthorhombic $SrIrO_3$ thin films, J. Mater. Res. **29**, 2491 (2014).

[26] A. Biswas and Y. H. Jeong, Effects of substrate temperature on the unusual non-Fermi liquid metal to insulator transition in perovskite $SrIrO_3$ thin films, J. Phys. D Appl. Phys. **48**, 135303 (2015).

[27] Y. F. Nie, P. D. C. King, C. H. Kim, M. Uchida, H. I. Wei, B. D. Faeth, J. P. Ruf, J. P. C. Ruff, L. Xie, X. Pan *et al.*, Interplay of spin-orbit interactions, dimensionality, and octahedral rotations in semimetallic $SrIrO_3$, Phys. Rev. Lett. **114**, 016401 (2015).

[28] K. R. Kleindienst, K. Wolff, J. Schubert, R. Schneider, and D. Fuchs, Structural properties and anisotropic electronic transport in $SrIrO_3$ films, Phys. Rev. B **98**, 115113 (2018).

[29] See Supplemental Material at http://link.aps.org/supplemental/10.1103/PhysRevB.111.075142 for sample preparation, structural characterization, and data analysis.

[30] A. M. Glazer, The classification of tilted octahedra in perovskites, Acta Cryst. B **28**, 3384 (1972).

[31] P. E. R. Blanchard, E. Reynolds, B. J. Kennedy, J. A. Kimpton, M. Avdeev, and A. A. Belik, Anomalous thermal expansion in orthorhombic perovskite $SrIrO_3$: Interplay between spin-orbit coupling and the crystal lattice, Phys. Rev. B **89**, 214106 (2014).

[32] K. Samanta, F. M. Ardito, N. M. Souza-Neto, and E. Granado, First-order structural transition and pressure-induced lattice/phonon anomalies in Sr_2IrO_4, Phys. Rev. B **98**, 094101 (2018).

[33] C. Chen, Y. Zhou, X. Chen, T. Han, C. An, Y. Zhou, Y. Yuan, B. Zhang, S. Wang, R. Zhang *et al.*, Persistent insulating state at megabar pressures in strongly spin-orbit coupled Sr_2IrO_4, Phys. Rev. B **101**, 144102 (2020).

[34] D. Fuchs, A. K. Jaiswal, A. A. Haghighirad, F. Wilhelm, A. Rogalev, and M. Le Tacon, Electronic and magnetic structure of $SrIro_3/LaCoO_3$, superlattices, ESRF experimental report HC-5007, March (2023).

[35] S. J. Moon, M. W. Kim, K. W. Kim, Y. S. Lee, J.-Y. Kim, J.-H. Park, B. J. Kim, S.-J. Oh, S. Nakatsuji, Y. Maeno *et al.*, Electronic structures of layered perovskite Sr_2MO_4 (M = Ru, Rh, and Ir), Phys. Rev. B **74**, 113104 (2006).

[36] M. Moretti Sala, M. Rossi, A. Al-Zein, S. Boseggia, E. C. Hunter, R. S. Perry, D. Prabhakaran, A. T. Boothroyd, N. B. Brookes, D. F. McMorrow *et al.*, Crystal field splitting in $Sr_{n+1}Ir_nO_{3n+1}$ ($n = 1, 2$) iridates probed by x-ray Raman spectroscopy, Phys. Rev. B **90**, 085126 (2014).

[37] H. Gretarsson, N. H. Sung, M. Höppner, B. J. Kim, B. Keimer, and M. Le Tacon, Two-magnon Raman scattering and pseudospin-lattice interactions in Sr_2IrO_4 and $Sr_3Ir_2O_7$, Phys. Rev. Lett. **116**, 136401 (2016).

[38] J. Kim, D. Casa, M. H. Upton, T. Gog, Young-June Kim, J. F. Mitchell, M. van Veenendaal, M. Daghofer, J. van den Brink, G. Khaliullin *et al.*, Magnetic excitation spectra of Sr_2IrO_4 probed by resonant inelastic x-ray scattering: Establishing links to cuprate superconductors, Phys. Rev. Lett. **108**, 177003 (2012).

[39] B. Andlauer, J. Schneider, and W. Tolksdorf, Optical absorption, fluorescence, and electron spin resonance of Ir^{4+} on octahedral sites in $Y_3Ga_5O_{12}$, Physica Status Solidi (b) **73**, 533 (1976).

[40] G. L. Stamokostas and G. A. Fiete, Mixing of t_{2g}-e_g orbitals in 4*d* and 5*d* transition metal oxides, Phys. Rev. B **97**, 085150 (2018).

[41] M. A. Laguna-Marco, D. Haskel, N. Souza-Neto, J. C. Lang, V. V. Krishnamurthy, S. Chikara, G. Cao, and M. van Veenendaal, Orbital magnetism and spin-orbit effects in the

electronic structure of $BaIrO_3$, Phys. Rev. Lett. **105**, 216407 (2010).

[42] B. T. Thole, G. van der Laan, J. C. Fuggle, G. A. Sawatzky, R. C. Karnatak, and J.-M. Esteva, $3d$ x-ray-absorption lines and the $3d^9\,4f^{n+1}$ multiplets of the lanthanides, Phys. Rev. B **32**, 5107 (1985).

[43] M. A. Zeb and H.-Y. Kee, Interplay between spin-orbit coupling and Hubbard interaction in $SrIrO_3$ and related *Pbnm* perovskite oxides, Phys. Rev. B **86**, 085149 (2012).

[44] A. de la Torre, S. McKeown Walker, F. Y. Bruno, S. Riccó, Z. Wang, I. Gutierrez Lezama, G. Scheerer, G. Giriat, D. Jaccard, C. Berthod *et al.*, Collapse of the Mott gap and emergence of a nodal liquid in lightly doped Sr_2IrO_4, Phys. Rev. Lett. **115**, 176402 (2015).

[45] R. Arita, J. Kuneš, A. V. Kozhevnikov, A. G. Eguiluz, and M. Imada, *Ab initio* studies on the interplay between spin-orbit interaction and Coulomb correlation in Sr_2IrO_4 and Ba_2IrO_4, Phys. Rev. Lett. **108**, 086403 (2012).

[46] C. Donnerer, Z. Feng, J. G. Vale, S. N. Andreev, I. V. Solovyev, E. C. Hunter, M. Hanfland, R. S. Perry, H. M. Rønnow, M. I. McMahon *et al.*, Pressure dependence of the structure and electronic properties of $Sr_3Ir_2O_7$, Phys. Rev. B **93**, 174118 (2016).